Single-Photon Synchronous Detection

Cristiano Niclass, *Member, IEEE*, Claudio Favi, Theo Kluter, Frédéric Monnier, and Edoardo Charbon, *Member, IEEE*

***Abstract*—Phase and intensity of light are detected simultaneously using a fully digital imaging technique: single-photon synchronous detection. This approach has been theoretically and experimentally investigated in this paper. We designed a fully integrated camera implementing the new technique that was fabricated in a 0.35 μm CMOS technology. The camera demonstrator features a modulated light source, so as to independently capture the time-of-flight of the photons reflected by a target, thereby reconstructing a depth map of the scene. The camera also enables image enhancement of 2D scenes when used in passive mode, where differential maps of the reflection patterns are the basis for advanced image processing algorithms. Extensive testing has shown the suitability of the technique and confirmed phase accuracy predictions. Experimental results showed that the proposed rangefinder method is effective. Distance measurement performance was characterized with a maximum nonlinearity error lower than 12 cm within a range of a few meters. In the same range, the maximum repeatability error was 3.8 cm.**

***Index Terms*—Single-photon synchronous detection, solid-state 3D imaging, 3D image sensor, 3D camera, flash camera, time-of-flight, rangefinder, range imaging, depth sensor, single-photon detector, avalanche photodiode, SPAD, SPSD.**

I. Introduction

COMBINED intensity and phase of multi- or monochromatic light carry more information than simple intensity. It can be used to infer several properties of the material it was reflected by. It can also be used to determine the position of the reflecting target using optical rangefinding, where the time-of-flight (TOF) of a reflected beam of light is computed from the phase difference between an outgoing and an incoming optical signal. The techniques traditionally used in the evaluation of the phase of light pulses with respect to the outgoing source are conceptually based on homodyne and heterodyne demodulators in radio frequency receivers, whereas the incoming radio signal is replaced by the optical signal impinging upon the detector. In these devices, the local oscillator is an electrical or optical signal synchronized with the outgoing modulated light source. The two signals are mixed and low-pass filtered, generally *in situ*, i.e., at pixel-level, to obtain an intermediate frequency or baseband signal proportional to the phase difference between outgoing and incoming light.

This technique has been applied successfully to CCD [1]–[3] and CMOS [4]–[6] processes and products based on this technology have been commercially available for some time now. Pixel-level mixing is performed during a light modulation cycle by selectively redirecting photocharges that are partially in and out of phase onto different locations for accumulation. The precision with which carriers are selectively redirected toward the correct accumulation site is limited by a relatively slow diffusion process below the photogate. As a result, time resolution is also limited for each modulation cycle. Moreover, the relatively small number of charges involved in each measurement cycle requires one to average the measurement over a very large number of cycles, typically in the millions, to reduce the impact of shot noise and other non-idealities. Hence, the accumulation process and consequent TOF evaluation typically takes tens of milliseconds.

CCD and CMOS rangefinders have been improved over the years to reach time resolutions up to a few nanoseconds for CCD/CMOS [7]. Nonetheless, these methods still suffer from the analog nature of the phase signal and the inevitable analog processing and A/D conversion it ultimately requires. The latter adds sources of error and increases the chip complexity. In the analog approach background illumination can be eliminated by virtue of the fact that it appears as a common-mode signal in each detector. However, when saturation is reached, the differential output signal proportional to the phase difference between outgoing and incoming light wave begins to compress, thus causing background effects to resurface and contrast to be slashed.

This paper reports on the first fully digital, multi-pixel approach to phase detection based on single-photon avalanche diodes (SPADs); we call it single-photon synchronous detection (SPSD). In SPSD, a single photon detected by a SPAD triggers a digital pulse that increments a counter that replaces the accumulating diffusion. The charge redirection in conventional analog methods, in turn, is replaced by a simple demultiplexer. The phase can thus be computed digitally for each pixel in a straightforward manner.

The advantages of SPSD over conventional photogate-based phase demodulation methods are at several levels. First, the time resolution of a partial phase measurement during a modulation cycle is far superior, since it is dominated by the time resolution of a SPAD, typically a few tens of picoseconds [8]. Thus, in principle a much smaller number of cycles is sufficient to achieve the same overall phase accuracy. Second, due to the digital nature of the phase measurement, no errors are introduced during the accumulation period, except for unavoidable photon shot noise. The lack of analog amplification and A/D conversion removes

Manuscript received November 06, 2008; revised February 09, 2009. Current version published June 24, 2009. This work was supported in part by a grant in the framework of the Innovation Network initiative from EPFL (Innogrant).

C. Niclass was with the Ecole Polytechnique Fédérale de Lausanne (EPFL), Lausanne, Switzerland. He is now with Toyota Central R&D Labs Inc., Aichi 480-1192, Japan (e-mail: niclass@mosk.tytlabs.co.jp).

C. Favi, T. Kluter, and F. Monnier are with the Ecole Polytechnique Fédérale de Lausanne (EPFL), CH-1015 Lausanne, Switzerland.

E. Charbon is with the TU Delft, 2628 CD Delft, The Netherlands.

Color versions of one or more of the figures in this paper are available online at http://ieeexplore.ieee.org.

Digital Object Identifier 10.1109/JSSC.2009.2021920

quantization errors and the usual non-idealities associated with these components. Third, SPSD inherently prevents signal compression in saturation. This is achieved by virtue of the digital nature of counters that can easily detect when the maximum counting range is reached via the overflow bit. In SPSD that bit is used, on a pixel-by-pixel basis, to stop accumulation in all the counters involved in the detection. Unlike global saturation control techniques (such as e.g., [6]), overflow detection is both simple and accurate, and it can be performed digitally with a simple feedback gate. Fourth, the device is amenable to implementing multiple access techniques to enable coexisting rangefinding systems in close proximity based, for example, on FDMA or CDMA [9].

SPSD was implemented in a camera fabricated in 0.35 μm CMOS technology. The core of the camera is an array of 60×48 fully scalable SPSD pixels with a pitch of 85 μm. The camera takes advantage of full pixel parallelism, as accumulation is performed in all the pixels *simultaneously* and *independently*. In addition, the sensor is highly photon efficient since the vast majority of the time is used to capture light while an insignificant portion of time is used for reading out the pixel contents and zero time is used for conversions of any kind. Thus in principle, no photons impinging upon the detector active area are lost, if separated by at least the dead time of a SPAD. This is a significant development with respect to recent implementations of SPAD arrays [10], [11] based on the time-correlated single-photon counting (TCSPC) technique [12].

The camera was yielded a resolution of approximately 3.8 cm, at a distance of 2.4 meters, with a frame rate of 22 fps when tested on a TOF rangefinder setup in combination with an array of LEDs operating at 30 MHz with a mean optical power of 800 mW. The modulation waveform used in the experiment was sinusoidal and the maximum range of our experiments was 5 m, whereas higher ranges could be obtained using either lower modulation frequencies or techniques for ambiguity resolution.

II. Single-Photon Synchronous Detection

The SPSD technique, introduced in [9], [13], involves the demodulation of the phase shift an optical signal experiences when travelling from source to target and back to the sensor. Fig. 1 shows the basic setup involved in a solid-state 3D imager based on SPSD. It consists of a periodically modulated light source, typically a sine wave, used to illuminate the target, imaging optics, a bandpass filter used to block background light, and a single-photon image sensor. This sensor comprises an array of pixels with single-photon detection and an on-pixel demodulation circuitry. Depending upon the waveform used, the optical signal spectrum may contain more than a single harmonic. However, similarly to photogate-based lock-in pixels, such as [3], the SPSD rangefinder computes the phase of the first harmonic only. We thus assume that the relevant back-reflected light signal received by the detector is characterized by a sine wave with amplitude A, offset B, fundamental frequency of modulation f_0, and a phase difference with respect to the outgoing light intensity φ. Back-reflected photons are imaged onto the array of pixels at the focal plane. In each pixel, a SPSD circuit performs

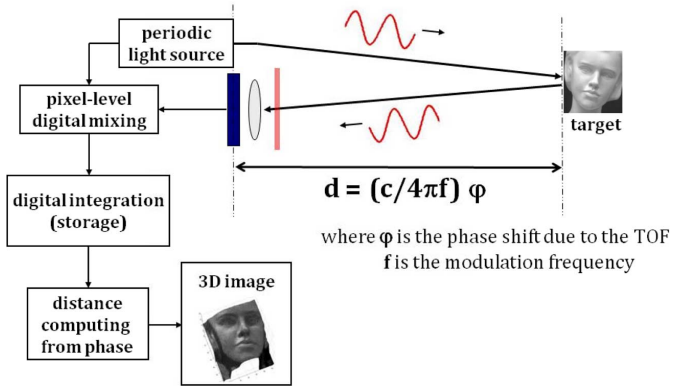

Fig. 1. Solid-state 3D imaging setup based on SPSD.

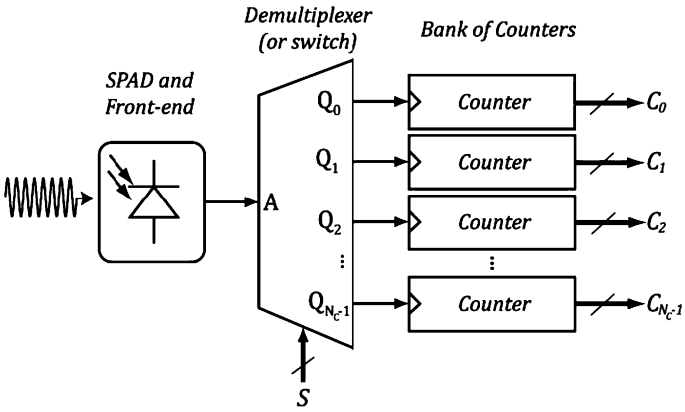

Fig. 2. SPSD pixel architecture. A single-photon detector and its front-end circuit are used to detect individual photons.

the demodulation of φ, A, and B. Once the phase is determined, distance z may be independently computed in each pixel as

$$z = \frac{c}{2}\frac{\varphi}{2\pi f_0}. \tag{1}$$

The general in-pixel SPSD demodulation circuit is shown in Fig. 2. The SPSD demodulation principle involves a synchronous detection and sampling of the incident photon flux. A single-photon detector and its front-end circuit are used to detect individual photons. At the output of the front-end circuit, discrete digital pulses resulting from photon detections are accurately generated. A demultiplexer redistributes the pulses to N_{C} counters via control signal S which is digitally selecting all the counters in sequence and in synch with the illumination source. Explicitly, signal demodulation is achieved by dividing each period of the illumination signal in N_C uniform time intervals, namely $\Delta T_0, \Delta T_1, \ldots, \Delta T_{\mathrm{k}}, \ldots, \Delta T_{\mathrm{NC}-1}$. At the end of the integration period, every counter stores a value C_{k} corresponding to the counted photons in the corresponding time intervals $\Delta T_0, \Delta T_1, \ldots, \Delta T_{\mathrm{k}}, \ldots, \Delta T_{\mathrm{NC}-1}$, respectively.

Since the SPSD demodulation is carried out over a large number of illumination cycles, the distribution of counter contents converges to the incident optical signal waveform over a single period. This principle is shown in Fig. 3 where the number of counters (N_{C}) is assumed to be 4 and the light source sinusoidal. In the picture, $P_{\mathrm{S}}(t)$ represents the incident optical power onto the single-photon detector of a given pixel.

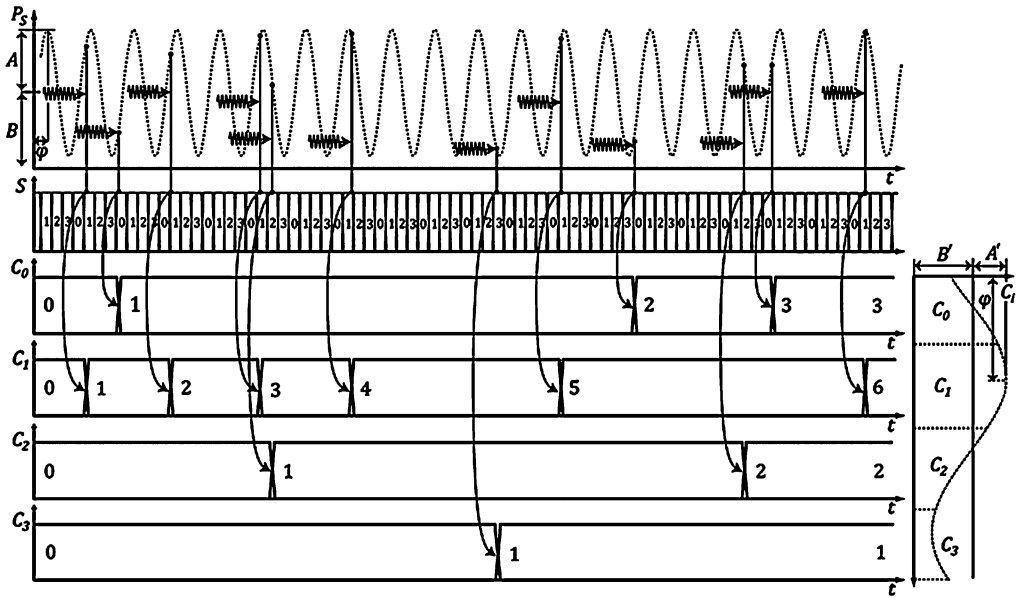

Fig. 3. Waveform of SPSD demodulation signals for a pixel based on four counters. P_{S} is the incident optical power, which is proportional to the incident photon flux, S is the demultiplexer selection signal, and C_0, C_1, C_2, and C_3 are the counter values. Note that, over time, the distribution of the counter values converges to the incident power waveform within one period.

In the picture, 20 signal periods are illustrated. Note that the sinusoidal waveform of P_{S} is an ideal representation. In fact, since the incident optical power that enters the active area of the single-photon detector is extremely low, P_{S} is a collection of discrete photonic events that follows a sinusoidal distribution in time. In most cases, many periods of P_{S} do not contain any photon and periods with more than a single photon are rare. In the picture, the first photon detection occurs in the second period. Since state of S at that moment was 1, counter C_1 was incremented. Similarly, on the second photon detection, the state of S was 0, thus resulting in the increment of C_0. Note that, as the number of detected photons increases, the distribution of the counter values tends towards the mean value of P_{S} over one period, shown in the right-hand side of the picture.

Thanks to the digital nature of single-photon detectors, phase demodulation may be achieved in a fully digital implementation. Note that the demultiplexer may be replaced by a simple switch. However, taking into account the nature of the signals involved, a fully digital implementation leads to the best performance for a given silicon area budget. Furthermore, in the illustration of the SPSD principle, no assumption was made with respect to the depth of the counters that are assumed ideal for now. Although the acquisition of A, B, and φ in SPSD differs considerably from that of CCD/CMOS lock-in sensors based on photogates, the post-processing to obtain depth information is identical. Unlike CCD/CMOS lock-in pixels however, in SPSD, the acquisition of $\{C_{\mathrm{k}}\}$ does not involve any analog processing or analog-to-digital conversion, thus leading to a virtually noise free detection and demodulation approach.

In Appendix A, the amplitude A', the offset B', and the phase φ of the sampled waveform are derived in the general case of N_{C} counters. Assuming $N_{\mathrm{C}} = 4$ and the phases associated to each counter to be uniform at 0, 90, 180, and 270 degrees, parameters A', B', and φ are computed from $\{C_{\mathrm{k}}\}$ in each pixel as follows:

$$A' = \frac{\sqrt{(C_{270} - C_{90})^2 + (C_0 - C_{180})^2}}{2}, \tag{2}$$

$$B' = \frac{C_0 + C_{90} + C_{180} + C_{270}}{4}, \tag{3}$$

$$\varphi' = \arctan\left(\frac{C_{270} - C_{90}}{C_0 - C_{180}}\right). \tag{4}$$

These Equations were originally described in [1], for CCD lock-in pixels. The four-sample case is a very good compromise between high demodulation contrast and pixel complexity, whereby demodulation contrast c_{D} is defined as (see Appendix A)

$$c_D = \mathrm{sinc}\left(\pi \frac{\Delta T}{T_0}\right) \tag{5}$$

where ΔT is the sampling interval for each counter and $T_0 = 1/f_0$. Note that, for a pure sinewave illumination, it is required that at least three samples be implemented to respect the Nyquist-Shannon sampling theorem. In the case of four samples, and assuming a ΔT of $T_0/4$ as illustrated in Fig. 3, the demodulation contrast c_{D} is 90%. For example, if eight samples are implemented $(N_{\mathrm{C}} = 8)$ with ΔT of $T_0/8$, then c_{D} becomes 97.4%. That is, an efficiency improvement of 7% at the price of approximately 100% of increase in circuit area at pixel-level.

Although phase φ is the most important result for a TOF rangefinder, A' and B' also carry interesting pixel information. A' may be conveniently used to determine whether a pixel signal, in a given acquisition frame, has a sufficiently strong

amplitude, so as to be considered as a reliable measurement. Indeed, pixel signals with negligible amplitude could be simply disregarded. B' may also be used to compute intensity images.

III. Modeling Performance in SPSD

Our reasoning in the modeling of performance in SPSD was inspired by previous work in lock-in detectors, e.g., [1], [14]. However, the digital nature of SPSD and the notable lack of most of the noise sources and non-idealities plaguing conventional lock-in detectors make this analysis new.

A. Distance Resolution

Rangefinding precision in SPSD may be derived from (1) to depend on design or environment parameters. The r.m.s. distance resolution σ_{Error} is expressed as

$$\sigma_{\mathrm{Error}} = \frac{R_D}{2\pi}\sigma_\varphi \tag{6}$$

where σ_φ is the 1σ phase error and R_{D} is the non-ambiguous distance range, computed as

$$R_D = \frac{c}{2f_0}. \tag{7}$$

In [14], an expression for σ_φ was determined by propagating the errors of the sample values $\{C_k\}$ into φ, using the following formula:

$$\sigma_\varphi^2 = \sum_{k=0}^{N_C-1}\left|\frac{\partial\varphi}{\partial C_k}\right|^2\sigma_{C_k}^2 \tag{8}$$

where $\sigma_{C_{\mathrm{k}}}^2$ is the variance of C_k., i.e., the counted value in counter k. In SPSD, assuming that the intervals $\Delta T_0, \Delta T_1, \ldots, \Delta T_{\mathrm{NC}-1}$ are uniform, which may be enforced by design, $\{C_{\mathrm{k}}\}$ are statistically independent. Note that $\{C_{\mathrm{k}}\}$ is a collection of random variables that are in turn affected by a number of noise sources. Nonetheless, since the integration and readout of $\{C_{\mathrm{k}}\}$ are virtually noiseless, the main noise contributions are limited to photon shot noise and dark count rate (DCR), the dominating noise sources in single-photon detectors. Furthermore, given that the number of photon detections and the number of dark counts integrated over time are well approximated by Poisson variables, $\{C_{\mathrm{k}}\}$ may also be assumed to be a collection of Poisson random variables. Consequently, the variance of C_{k} is given by their mean value. Note that since (4) is nonlinear, 3rd -order and higher moments of C_{k} are assumed to be negligible in (8). This is a very reasonable assumption when the mean value of C_{k}, i.e., the mean number of detected events, is higher than a certain value. For example, when the mean value of C_{k} is greater than 100, its 3rd -order and 4th -order moments are lower than 0.1% and 0.01% of its variance, respectively. In the case of four samples per period, i.e., $N_{\mathrm{C}} = 4$, (6) may be rewritten as a function of A' and B' as

$$\sigma_{\mathrm{Error}} = \frac{R_D}{\sqrt{8}\pi}\frac{\sqrt{B'}}{A'}. \tag{9}$$

In (9), quantities A' and B' may be computed as a function of demodulation contrast c_D, integration time T, and photon counting rates S_R and B_R. Terms S_R and B_R are the mean photon counting rates due to the illumination and background light, respectively. Thus,

$$\sigma_{\mathrm{Error}} = \frac{R_D}{\sqrt{8}\pi c_D c_S}\frac{1}{\sqrt{T\cdot \mathrm{SBR}\cdot S_R}} \tag{10}$$

where c_S is the signal modulation contrast due to non-idealities in the illumination source and SBR is the ratio between signal to background photon counting rates. In (10), the contribution of DCR was conveniently ignored, as it is typically negligible compared to the background count rate. In situations where this assumption does not hold, a general expression for the distance resolution is given by

$$\sigma_{\mathrm{Error}} = \frac{R_D}{\sqrt{8}\pi c_D c_S S_R}\sqrt{\frac{B_R+\mathrm{DCR}}{T}}. \tag{11}$$

In [15], a model that relates environmental, device, circuit, and system parameters to actual photon counting rates (S_R and B_R) is proposed and may be effectively utilized with (10) to assess system performance.

B. Nonlinearity Errors

Similarly to photogate lock-in pixels, SPSD may also suffer from nonlinearity errors. These errors are mostly due to harmonic distortion in the illumination source, which cause aliasing errors. However, since neither analog processing nor conversion is required in SPAD image sensors, typical errors that cause nonlinearity in analog signals do not affect the SPSD demodulation. Examples of analog non-idealities are gain nonlinearity, gain non-uniformity in pixels, ADC nonlinearity, full-well saturation, etc. In SPSD, under some conditions of non-saturation, the demodulation process is nearly ideal. Saturation effects in SPSD exist though and may be divided in three categories: (i) saturation due to limited integrator capacity, (ii) saturation due to pile-up effect, and (iii) saturation due to SPAD dead time which affects dynamic range. The saturation effect due to limited integrator capacity is effectively addressed by design techniques. Note that the equivalent in SPSD of photogate full-well capacity is simply the counter depth. Counters are typically digital circuits and their depth (capacity) may be increased easily using standard design techniques. The remaining nonlinearity-related issues are described in the next paragraphs.

C. Aliasing Errors

The sampling nature of SPSD demodulation inherently assumes incident optical signals with restricted bandwidth. This is particularly true if one takes into account the lack of low-pass filter prior to the sampling operation. Consequently, aliasing issues are dealt with during the design of the illumination system. Assuming that a perfect sinusoidal illumination system is utilized, more than two samples per period are required in SPSD to prevent aliasing, according to Nyquist-Shannon sampling theorem.

Typically, a SPSD pixel may provide four $\{C_k\}$ values, i.e., four samples per period. As a result, no aliasing effects occur and the measurement characteristic is perfectly linear. However, in practice, it is difficult to build illumination systems that exhibit only the fundamental frequency. The main reason for this is the linearity requirement in LED or LD drivers. In order to build low-cost and low-power arrays of LED/LD drivers, typically nonlinear circuit topologies such as push-pull amplifiers are utilized. As a result, the illumination signals usually exhibit harmonic distortions that are sampled by the SPSD principle, thus leading to nonlinearity errors due to aliasing. Note that this effect also occurs in conventional lock-in pixels. Fortunately, thanks to the availability of four (or more) $\{C_k\}$ per pixel, these errors are partially mitigated.

A quantitative analysis of aliasing effects for a number of potential illumination waveforms is presented by Lange [14]. Table I gives a summary of the maximum nonlinearity errors for typical illumination waveform. The results of the table are based on $N_C = 4$ and $\Delta T = T_0/2$. The demodulation based on four samples is affected by nonlinearity errors that can be as high as 5.4% when the 3rd harmonic is present in the illumination signal. However, as demonstrated in [14], even harmonics do not impact linearity at all. This is due to the fact that the sampling window is a square-wave in time domain, thus leading to a *sinc* function in the frequency domain with zeros in correspondence to even multiples of the sampling frequency. From an illumination system design standpoint, it would be convenient to utilize square wave illumination as digital drivers provide cheap and power-efficient solutions. Nonetheless, as can be seen in Table I, such solution leads to nonlinearity errors that are as high as 1.7%. A clear compromise should therefore be found in terms of harmonic distortion versus illumination power efficiency (and cost).

TABLE I
MAXIMUM NONLINEARITY ERRORS DUE TO ALIASING IN SPSD DEMODULATION FOR A NUMBER OF ILLUMINATION WAVEFORMS

Illumination Waveform	Harmonics	Maximum Non-Linearity Errors [%]
$cos(\omega_0 t)$	1	0
$cos^2(\omega_0 t)$	1	0
$cos(\omega_0 t) + cos(2\omega_0 t)$	1, 2	0
$cos(\omega_0 t) + cos(3\omega_0 t)$	1, 3	±5.4
$cos(\omega_0 t) + cos(4\omega_0 t)$	1, 4	0
$cos(\omega_0 t) + cos(5\omega_0 t)$	1, 5	±3.2
$cos(\omega_0 t) + cos(6\omega_0 t)$	1, 6	0
$cos(\omega_0 t) + cos(7\omega_0 t)$	1, 7	±2.2
Square wave: $\sum_{m=0}^{\infty} \frac{sin\left((2m+1)\omega_0\left(t+\frac{T_0}{4}\right)\right)}{2m+1}$	1, 3, 5, 7, …	±1.7

D. Pile-Up Distortion

A very important assumption in TCSPC is that, on average, less than a photon should be detected per illumination cycle [12], [15]. When this condition is not met, the measured histogram experiences distortion. This is commonly known as pile-up and its effects may also impair SPSD performance. In particular, asymmetric distortions of the counter outputs may impact measurement linearity of the phase.

To analyze the effects of pile-up let us define parameter M that represents the mean number of photon detections per illumination period

$$M = \frac{\frac{\lambda_{SG}\bar{P}_S}{hc}\eta_{SPAD}}{f_0} \tag{12}$$

where λ_{SG} is the illumination wavelength, η_{SPAD} is the SPAD photon detection probability, $\bar{P}_s$ is the mean value of the signal optical power impinging the SPAD active area, h is Planck's constant, c is the speed of light, and f_0 is the modulation frequency.

Pile-up distortion is clearly noticeable when M is higher than 1. Please refer to the pile-up model described in [15] for a quantitative evaluation. In short-range measurements, the modulation period T_0 is comparable or shorter than typical values of SPAD dead time, i.e., 20 to 40 nanoseconds. As a result, when M is close to 1, the SPAD image sensor is at the limit of its saturation. This is as rather an exceptional region to operate in and it occurs only when the target is extremely close to the image sensor or it induces specular reflection. In those cases, the signal-to-background ratio SBR and the noise conditions are so favorable that parameterized correction for pile-up would be effective.

Note that only photons from the active illumination are taken into account in (12). Conversely, in long-range distances, T_0 is considerably longer than the dead time. In those cases, when objects are placed close to the image sensor (or induce specular reflection), M is likely to be higher than 1. However, when T_0 is longer than the dead time, distortion effects that are visible in pulsed illuminations, such as in TCSPC, tend to be negligible in sinusoidal modulation. The main reason for this is that in a sinusoidal wave, photons are randomly detected over the full period. Although the typical dead time applies upon each photon detection, when this process is averaged over a high number of cycles, the illumination waveform is eventually sampled rather uniformly over the period.

Independent of the sensors distance range, an effective solution to deal with pile-up is to prevent it by reducing the detector count rate, by controlling the SPAD's photon detection probability. This may be achieved electrically pixel-wise by adjusting the SPAD biasing. As a result, by insuring that the maximum count rate of a pixel is f_0 or a fraction of it, pile-up effects are eliminated. Note that pile-up effects only occur in pixels that exhibit high signal count rates. Most of pixels exhibit signal counting rates that are much lower than f_0. Those pixels benefit from the maximum detection efficiency.

E. Dynamic Range

The dynamic range (DR) is defined in SPAD-based imagers just as in conventional sensors, i.e., the maximum output swing divided by the temporal noise in the dark. The output swing is limited at the low end by the product of DCR and the integration

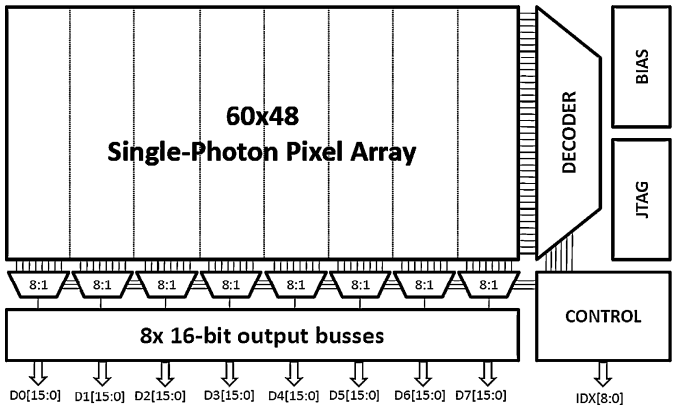

Fig. 4. Chip architecture. The sensor consists of a 60×48 pixel array, a JTAG controller, and fast parallel readout circuitry. Every pixel has two 8-bit counters with overflow prevention mechanism.

time. At the high end, the maximum count rate ever achieved by a SPAD is given by the inverse of dead time. As a result, the maximum achieved output value is expressed as the ratio of the integration time to the dead time. Finally, in the dark, the temporal noise is expressed by time-varying component of DCR. Since the number of dark counts detected in the integration time follows a Poisson distribution [8], its noise component is easily determined as

$$\begin{aligned} \mathrm{DR(dB)} &= 20 \cdot \log \left[\sqrt{\frac{T}{\mathrm{DCR}}} \left(\frac{1}{\mathrm{DT}} - \mathrm{DCR} \right) \right] \\ &\cong 20 \cdot \log \left(\sqrt{\frac{T}{\mathrm{DCR}}} \cdot \frac{1}{\mathrm{DT}} \right) \end{aligned} \tag{13}$$

where DT is the dead time of the SPAD. When evaluating (13) for typical parameters of CMOS SPADs in 0.35 μm, i.e., DCR of 600 Hz and DT of 40 ns, and for an integration time of 20 ms, the dynamic range of a SPAD image sensor was estimated at 107 dB. This result compares favorably with most of conventional CCD and CMOS image sensors, which typically exhibit DRs in the range of 60–75 dB.

IV. Image Sensor System Design

The design and characterization of the first fully integrated TOF 3D image sensor based on SPSD is described hereafter. For the first time, a large array of SPADs was implemented with fully parallel image acquisition and readout capability, enabling TOF measurements and intensity images at video rate. A simplified block diagram of the image sensor is shown in Fig. 4. It consists of an array of 60×48 single-photon pixels, each one comprising its own SPSD demodulation circuit based on two 8-bit counters. The sensor also includes a bias generation circuit, a boundary-scan testing (JTAG) controller for testing/characterization purposes, and a fast readout circuit.

A. Pixel Architecture

Single-photon detection at pixel level with high timing resolution is achieved by means of a 0.35 μm CMOS SPAD. Its

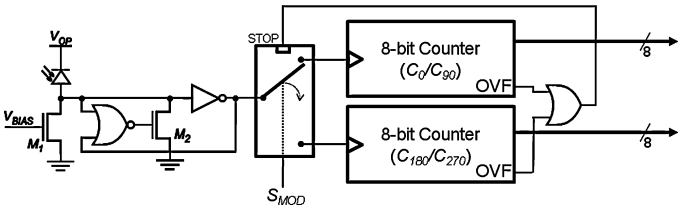

Fig. 5. Pixel architecture. Front-end, digital demodulation, and storage devices are the components of the pixel. Passive quenching and active recharge ensure higher dynamic range with little impact on pixel size. Fully digital implementation enables noise free demodulation and readout.

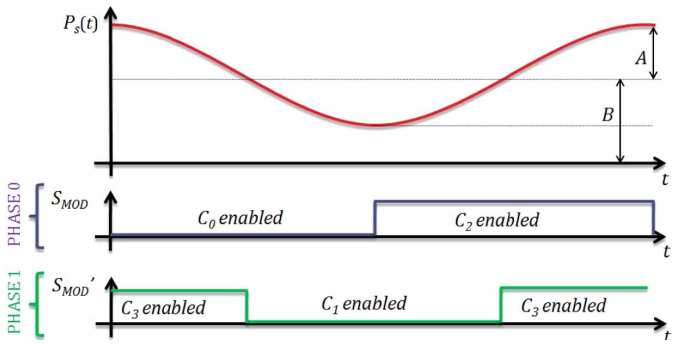

Fig. 6. Incident optical signal and demodulation waveforms.

front-end circuit involves 8 MOS transistors that perform passive quenching and active recharge, based on the dual-threshold scheme introduced in [15]. Fig. 5 shows the schematics of the complete pixel circuit. Active quenching is achieved by adequately choosing two different thresholds for the inverter and nor gates. At the inverter output, a digital inverted pulse reflects the detection of a photon. Its leading edge, i.e., high-to-low transition, accurately indicates the arrival time of the photon. As shown in Fig. 5, the demodulation circuit consists of a 2:1 multiplexer driven by a global signal S_{MOD}, synchronized with the light source driver, and two 8-bit counters. Each counter has a parallel tri-state output bus and a signal, OVF, indicating that the next increment would cause overflow. The OVF signals of both counters are ORed, so as to freeze the counters in the last state before overflow.

In order to unambiguously demodulate the signal phase, at least three counters are theoretically necessary. Practically, it is possible however to use only two counters and generate four samples. Fig. 6 shows an example of illumination waveform and demodulation waveforms, as adopted in this design. The sensor operates in an interlaced detection scheme based on two acquisition phases. In the first acquisition phase, the pixel-level demultiplexer switches between two counters so as to generate two samples, C_0 and C_2, corresponding to 0° and 180° phase with respect S_{MOD}. Once these two samples are acquired and readout, the sensor operates in the second acquisition phase, in which S_{MOD} is delayed by a quarter of period with respect to the reference signal. As a result, the same in-pixel counters are used to acquire samples C_1 and C_3, corresponding to 90° and 270° of phase. Note that, although only two counters are used, the demodulation circuit does not miss any photon detection, unless the counter maximum value is reached.

In our equations, we assume that all four samples $\{C_k\}$ are acquired simultaneously. When the objects in the scene are not static, the acquisition of four samples based on two counters may suffer from higher motion artifacts, than it would have if the four $\{C_k\}$ were acquired simultaneously. In order to solve this problem, the acquisition of C_0/C_2 and of C_1/C_3 should be interlaced at a sufficiently high frequency that moving objects appear static and thus affects all $\{C_k\}$ simultaneously. Note that conventional motion artifacts may persist depending on the actual frame rate achieved by the image sensor.

Based on this particular implementation, the sampling window duration ΔT was $T_0/2$, thus leading to a maximum demodulation contrast c_D of 64%, according to (5). This implementation achieves an interesting compromise between pixel size and overall demodulation contrast.

B. Readout

In this implementation, the readout circuit is based on a controller that allows the image sensor to operate autonomously, only requiring a single clock signal. As shown in Fig. 4, the pixel matrix area is divided in 8 blocks, each one consisting of 8×48 pixels and being handled by an independent readout block. The first and last readout blocks handle six active and two blocked columns each. A decoder, driven by the readout controller, selects a row. In that row, a pipelined sequence of readout and reset is achieved in the 8 blocks in parallel, thanks to the 8 digital output buses of 16 bits implemented. In each row, the readout sequence is operated as follows. The first pixels in all the 8 blocks are read out, then, when the second group of pixels in all the blocks are read out, the first ones are simultaneously reset to zero. When the readout circuit finishes reading out the eighth pixel group in all the blocks, it spends one additional cycle to reset them, before switching to the next row. As a result, 9 cycles of clock are necessary to read out and reset a full row. Since the sensor comprises 48 rows, the full frame rolling readout requires exactly 432 cycles. Note that in each readout cycle a digital signal, IDX[8:0], indicates the address of the pixels in the blocks that are currently being read out, and that each 16-bit bus outputs the contents of the two in-pixel counters simultaneously.

The readout circuit was designed to run at a clock frequency of up to 40 MHz. At that frequency, a frame acquisition and readout takes 10.8 μs. This time is short enough to be used in the interlaced acquisition of C_0/C_2 and C_1/C_3, thus preventing motion artifacts. Moreover, since a pixel may be read out and reset in only 10.8 μs, its 8-bit counters marginally reach their maximum values, assuming a dead time of 40 ns.

V. Experimental Results

A. Sensor Characterization

The image sensor described in this paper was fabricated in a 0.35 μm CMOS. The sensor, whose micrograph is shown in Fig. 7, has an area of 6.5×5.5 mm^2. Global distribution of S_{MOD} was implemented symmetrically, from a pad in the center of the top part of the pad ring. The image sensor was then mounted on a custom prototype of camera, based on a FPGA for data interface and USB controller to provide a link with any PC. The entire camera system prototype is shown in Fig. 8.

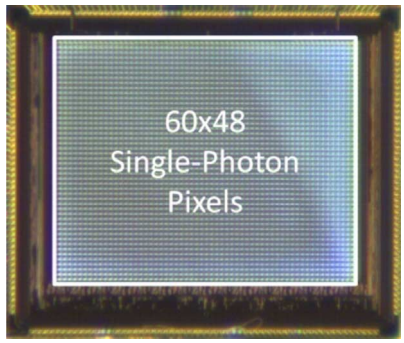

Fig. 7. Photomicrograph of the SPSD image sensor. The circuit, fabricated in 0.35 μm CMOS technology, has a surface of 6.5×5.5 mm^2. The pixel pitch is 85 μm.

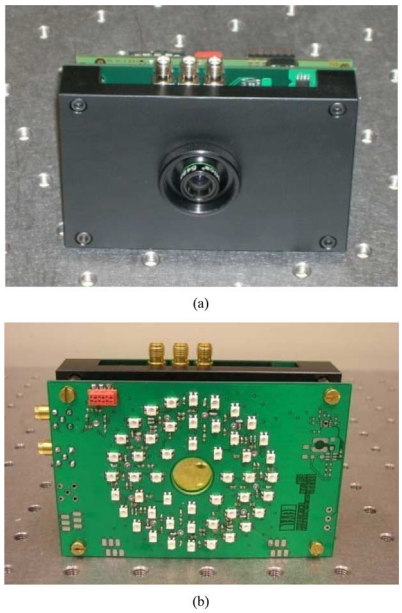

Fig. 8. Prototype of the SPSD camera: (a) camera casing without illumination system; (b) complete prototype. The 3D camera measures approximately $11 \times 7 \times 6$ cm^3.

The illumination system of the prototype is based on an array of 48 850 nm LEDs and it was specifically designed to fit on the camera prototype. Fig. 8(a) shows a picture of the prototype with the illumination system visible in the front. To prevent occlusion of the illumination beam, the array of LEDs was distributed along 3 concentric circles sharing the same center of the imaging lens. Moreover, to reduce the effects of multiple paths, from different LEDs, the outer LED circle was kept small. The illumination system was designed to emit a variable illumination power up to 800 mW in average, within a field of view of 50°. LED drivers may be operated at a maximum frequency of 40 MHz. Special placement and routing techniques were adopted for LEDs and drivers so as to prevent LED-to-LED timing skews. Moreover, thermal dissipation was handled with proper layout techniques as well as with adapted driver packages.

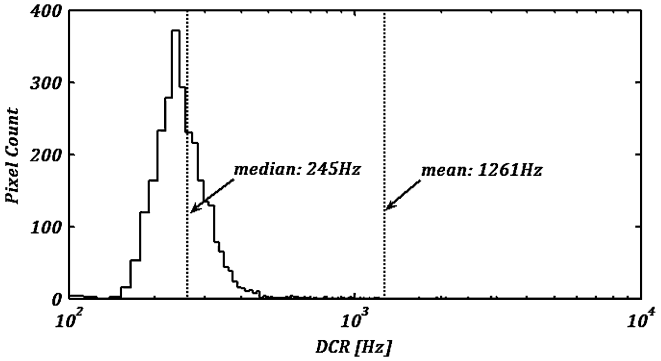

Fig. 9. DCR distribution over the array of SPADs. The median value was 245 Hz, whereas the mean value was relatively high, at 1.261 kHz, due to a small number of highly active pixels.

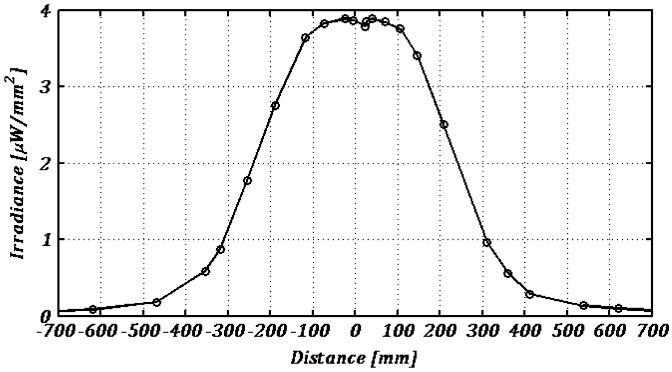

Fig. 10. Irradiance of illumination source as a function of off-axis distance, measured at 40 cm from the prototype. Assuming symmetry of revolution, the integral of the irradiance amounts to 800 mW of optical power.

The custom-made camera casing supports a C-mount lens or a M12-mount with adapter. For the characterization, we used an F/1.4 imaging lens mounted on a C-mount-to-M12 adapter. The imaging lens field-of-view was approximately 50°/40° (H/V) to match the illumination system field-of-view. In order to block a fraction of background light, a narrow-band interference optical filter centered at 850 nm was placed in front of the imaging lens. The FWHM of the filter was 40 nm.

Ranging characterization data were captured in indoor condition, under a measured background illuminance of 150 lux. The single-photon image sensor described in Section 4.4 was firstly tested and characterized. The SPAD front-end circuit, based on the dual-threshold passive quenching and active recharge circuit [15], was fully functional. The nominal dead time of 40 ns was set to operate in the 3D camera prototype. SPADs were characterized with respect to DCR. The distribution of DCR over all 3072 pixels in a chip sample is shown in Fig. 9. The median value in the 60×48 image sensor was 245 Hz, whereas the mean value was 1260 Hz. Similarly to previous SPAD imager implementations [8], [10], [11], higher mean value is mostly due to a small number of highly noisy pixels. Typically, in an imaging application, these pixels are deactivated without any impact to neighbor pixels.

B. Optical Components Characterization

The illumination system achieves the best compromise between modulation contrast (c_{S}) and operating frequency (f_0) when operated at 30 MHz. The system may be optionally set to operate at any frequency up to 40 MHz as well. However, as indicated by (11), distance repeatability errors decrease with the inverse of $c_{\mathrm{S}} f_0$ product. Note that distance range R_{D} is inversely proportional to f_0, according (7). As a result, it is important to increase the $c_{\mathrm{S}} f_0$ product to achieve the best precision within a given illumination power budget, provided that f_0 satisfies the range of interest. Consequently, experimental rangefinding performance was evaluated based on illumination repetition rate of 30 MHz.

In order to quantitatively determine the total optical power emitted by the camera prototype, a reference photodiode was utilized to scan the illumination beam at precisely 40 cm from the prototype. In order to determine the lateral displacement of the photodiode with respect to the center of the illumination beam, its distance with respect to a fixed reference was measured at each sampling point. Fig. 10 shows the distribution of illumination irradiance as a function of the off-axis distance. The measurements were carried out along a horizontal axis whose center coincides with the center of the illumination system. In view of the illumination topology, it is possible to assume symmetry of revolution so as to determine the total power. By numerically integrating the irradiance over the area and along the beam radius, a total illumination power of approximately 800 mW was determined.

As described earlier, a very important concern in the illumination system is harmonic distortion. The SPSD demodulation technique perfectly tolerates distortions in even harmonics, however, when odd harmonics exist, nonlinearity errors are expected. In the design of this illumination system, an important trade-off between power efficiency and distance accuracy exists. For a pure optical sine wave, linear components are required. Unfortunately, linear components are expensive and typically lead to poor electrical-to-optical conversion efficiency. As a result, the illumination prototype is based on a pseudo sinusoidal modulation, featuring nonetheless some harmonic distortions.

In order to experimentally evaluate the quality of the illumination waveform, a high-speed photodiode with a cut-off frequency of 500 MHz was utilized to sample the illumination beam. The photodiode output was analyzed on a 10 GS/s oscilloscope. The FFT of the measured waveform yielded the power spectral density (PSD) of Fig. 11. As can be seen in the plot, the 3rd harmonic power was approximately 27 dB lower than the fundamental frequency.

Finally, the illumination power actually measured by the 3D camera prototype also depends on the narrow-band interference filter placed in front of the image lens. In order to evaluate how much signal power is lost in the optical filter, a calibrated spectrometer was used to analyze the illumination optical spectrum at a fixed distance, along the optical axis. Once the illumination spectrum was measured, the 40 nm optical filter was carefully placed and aligned in front of the spectrometer (optic fiber) input, thus leading to filtered illumination spectrum. A plot of the original and filtered (normalized) optical PSD as a function of wavelength is shown in Fig. 12. The optical filter

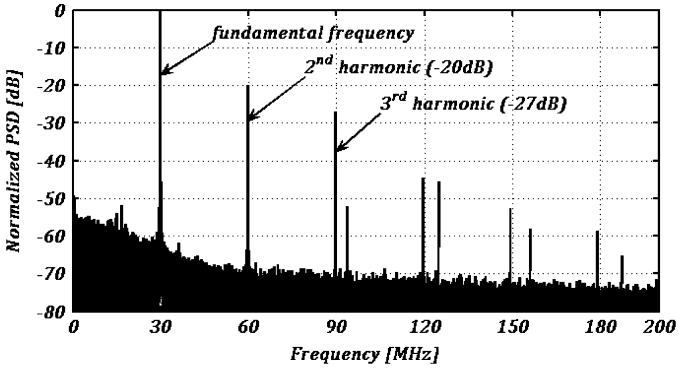

Fig. 11. Normalized PSD of illumination.

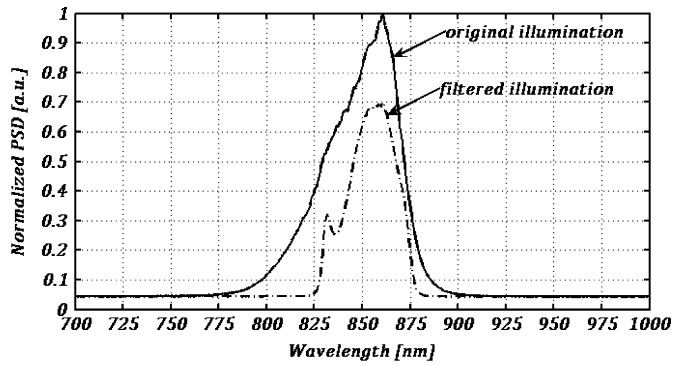

Fig. 12. Illumination optical spectrum measured with a spectrometer.

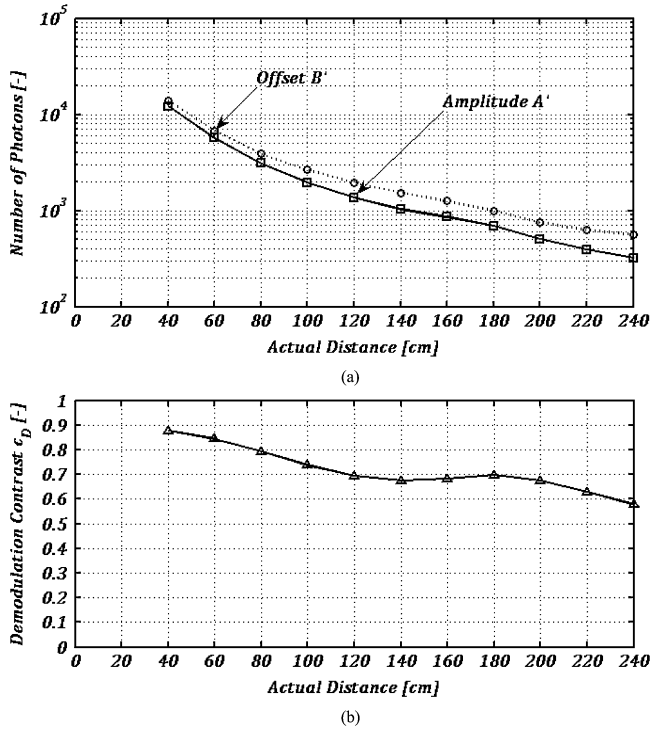

Fig. 13. (a) Recorded mean offset B and mean amplitude A, as a function of distance; (b) measured mean demodulation contrast c_{D} as a function of distance. Each distance measurement was statistically evaluated with 5000 samples using an integration time of 45 ms.

was effective in blocking light components out of the illumination band. However, it also had a negative impact on the actual signal power. The filter transmission at 850 nm was much lower than expected. Furthermore, the band-pass width of 40 nm also blocked an important fraction of the signal power. Nonetheless, experimental performance evaluation was based on this setup due to the unavailability of broader band-pass interference filters. The ratio of optical power integrated over the PSD between the filtered and non-filtered optical signals indicates the average filter transmission. It was only 56%, which shows that a large margin exists for improvement in signal gathering or in reducing illumination power consumption, keeping the performance reported here constant.

C. Rangefinding Performance

Quantitative evaluation of ranging performance was performed by statistically measuring distance error between the prototype and a reference panel, assumed as ground truth. The reference panel was carefully aligned in front of the camera prototype and its distance was varied from 40 cm up to 240 cm, in steps of 20 cm. In order to ensure accurate reference distances, an alternative measuring method was utilized. Systematic distance errors in the alignment and measurement of the reference plane were assumed to be within ± 3 mm. At each distance, 5000 measurements were computed and stored based on an integration time of 45 ms. This integration time leads to 22 frames per second.

In Fig. 13(a), the mean offset B' and amplitude A' are plotted as a function of distance. Fig. 13(b) shows a plot of the measured demodulation contrast. Both offset A' and B' follow a quadratic decay with the distance, especially in the beginning of the range. This implies that B' is mostly due to the active illumination, whose field-of-view of 50° leads to such quadratic decay in that range. This is particularly true in SPSD as demodulation is performed virtually free of noise, when background light and DCR are negligible. As can be seen in Fig. 13(b), the maximum achieved demodulation contrast is over 85%. Towards the end of the measurement range, the illumination signal is very weak and the background light component in B' causes c_{D} to decrease as a function of distance. However, it is still higher than 55% throughout the measurement range. High demodulation contrast was expected owing to excellent timing resolution of SPADs. However, one may note that 85% is higher than theoretical maximum c_{D} of 64%. The reason for this mismatch is that the theoretical c_{D} was based on a perfect sinusoidal waveform, whereas the actual illumination approaches a square waveform.

In Fig. 14(a), measured distance versus actual distance is plotted. Every distance indicated corresponds to the mean value over 5000 measurements. In Fig. 14(b), the mean error (μ_{Error}) with respect to ground truth is plotted, whereas 1σ repeatability error, i.e., σ_{Error}, is plotted in Fig. 14(c). Measured nonlinearity errors were higher than expected. However, these results compare favorably with nonlinearity performance of state-of-the-art 3D cameras based on CCD/CMOS lock-in pixels [16]. Similarly to [16], the main source of nonlinearity errors is given by aliasing effects due to higher harmonics in the illumination waveform. An improved illumination source is expected to reduce these errors. The maximum mean error was lower than 12 cm throughout the measurement range. It is

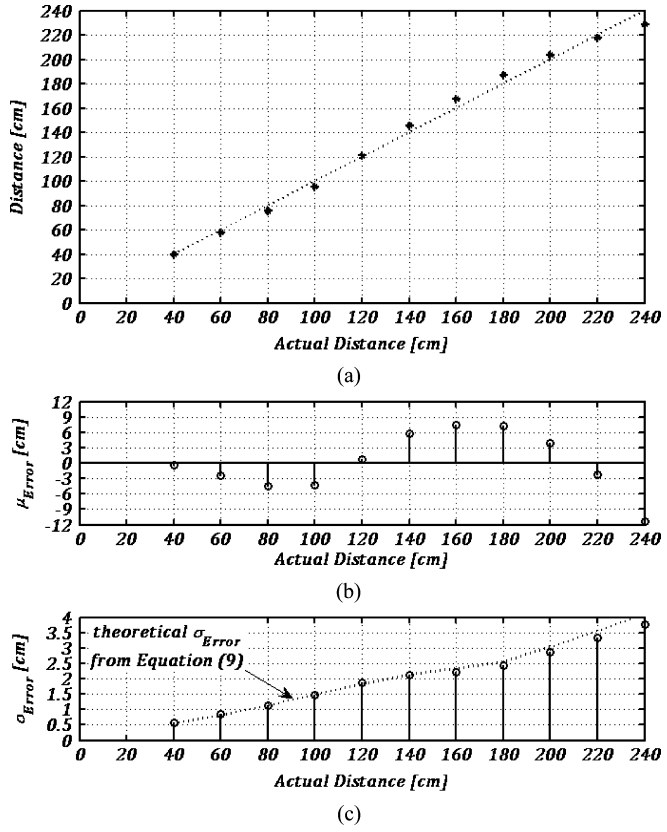

Fig. 14. Rangefinding performance of the proposed 3D camera prototype based on an implementation with $N_{\mathrm{C}} = 4$: (a) measured versus actual distance, compared to the ideal characteristic; (b) mean nonlinearity error as a function of distance; (c) actual and theoretical 1σ distance errors as a function of distance. Each distance was statistically evaluated with 5000 measurements using an integration time of 45 ms.

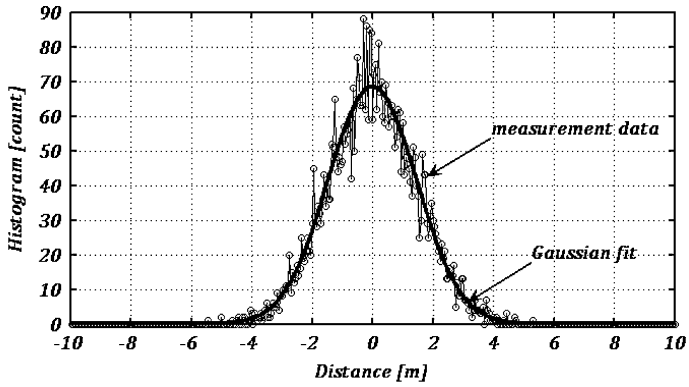

Fig. 15. Measurement error distribution using 5000 measurements at a distance of 1 m. Each measurement is based on a 45 ms integration time. In the plot, a comparison with a Gaussian fit is shown. The mean distance was subtracted from each measurement to show the symmetry of σ_{Error}.

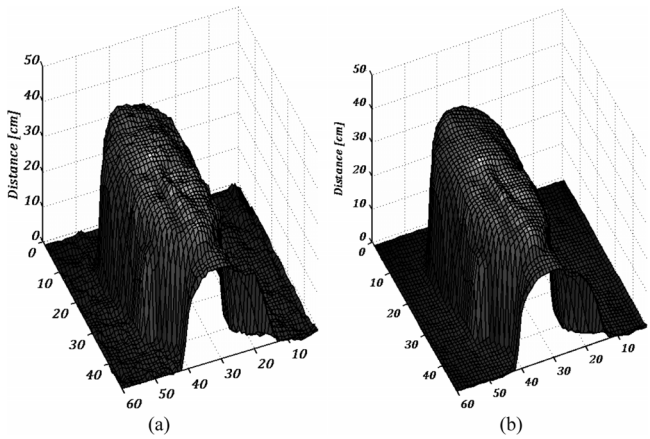

Fig. 16. Sample 3D images of a human-sized mannequin head acquired with two integration times: (a) 45 ms and (b) 450 ms. Depth axis is in cm.

below 8 cm within a range of 2 m. These errors may be reduced by means of parameterized correction algorithms.

Results of σ_{Error} were very close to performance predicted by theory, taking into account actual $A'A$ and $B'B$ values. This result validates the assumptions made to set (8). In particular, the fluctuations of $\{C_k\}$ due to photon shot noise clearly dominate over remaining sources of uncertainty such as SPAD timing resolution and electronic jitter. Interestingly, the measurement conditions led to an error that depends approximately linearly on the distance. A linear fit was computed from the data of Fig. 14(c), which indicates an increase of σ_{Error} at a pace of 1.51 cm per meter within the measurement range. In order to see the distribution of the error at a given distance, a histogram was built for the measurements taken at a distance of 1 m. Fig. 15 shows a plot of the measured histogram with a Gaussian fit. The mean distance error was subtracted from each measurement so as to build a histogram with zero mean. As can be seen, the random component of distance errors approaches a normal distribution relatively well. As a result, σ_{Error} is expected to improve by averaging similarly to a normal random variable.

Finally, the 3D camera prototype and SPSD technique were evaluated qualitatively by capturing 3D snapshots of several objects. Fig. 16(a) and (b) show two snapshots of a human-sized mannequin head, acquired with 45 ms and 450 ms of integration time, respectively. Fig. 17(a), (b), and (c) show sample 3D images of a table lamp acquired with 45 ms, 500 ms, and 1 s of integration time, respectively. The effects of averaging, when increasing the integration time, are clearly visible from the pictures.

In Table II, a summary of the performance achieved by the 3D camera prototype is listed. These results, demonstrate the suitability of the proposed SPSD technique. It also shows the performance that is achievable with a fully digital depth image sensor in CMOS technology.

VI. Conclusion

In this paper a novel method has been introduced for 3D image sensing. The method, called single-photon synchronous detection (SPSD), differs considerably from previous methods based on time-of-flight, in that it enables high precision in-pixel evaluation of phase-of-arrival of single photons. The core technology of the sensor is based on the single-photon avalanche diode (SPAD) technology implemented in a 0.35 μm CMOS process. Thanks to the use of a CMOS process, large arrays of pixels may be implemented, providing full parallelism in image acquisition, processing, and readout.

The approach has been theoretically and experimentally investigated in an array of 60×48 SPSD pixels, thus enabling

TABLE II
PERFORMANCE SUMMARY FOR THE SPSD BASED 3D IMAGE SENSOR

Parameter	***Value***	***Unit***
CMOS technology feature size	0.35	µm
SPAD image sensor resolution	60x48	-
SPAD active area	38	μm^2
SPAD median DCR	245	Hz
SPAD dead time	40	ns
Pixel pitch	85	µm
Imaging lens F-number	1.4	-
Illumination central wavelength	850	nm
Narrow band optical filter width	40	nm
Illumination frequency	30	MHz
Illumination field-of-view	50	°
Illumination average power	800	mW
Resolvable distance range	5	m
Integration time used in performance evaluation	45	ms
Chip power dissipation	35	mW
Maximum distance non-linearity error (μ_{Error}) up to 2.4m	11	cm
Maximum distance repeatability error (σ_{Error}) up to 2.4m	3.8	cm
Maximum feasible frame-rate [a),b)]	46296	fps

a) Assuming a complete SPSD demodulation per frame.
b) Currently not achieved due to prototype limitations.

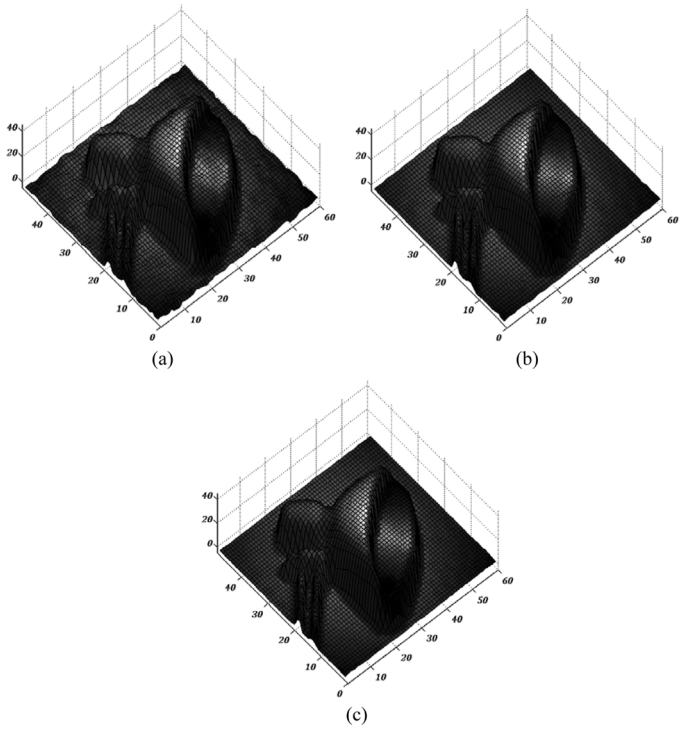

Fig. 17. Sample 3D images of a table light in front of a flat background acquired in (a) 50 ms, (b) 500 ms, and (c) 1 s of integration time. Depth axis is in cm.

real-time 3D image acquisition. A 3D camera prototype was designed and built based on the SPSD image sensor. Experimental results show that the SPSD rangefinder was effective, whereas a demodulation contrast as high as 85% was demonstrated. To the best of our knowledge, this value is superior than any demodulation contrast ever achieved using lock-in pixels in any technology, under the same conditions. Distance measurement performance was characterized with a maximum nonlinearity error of 11 cm within a range of 2.4 meters. In the same range, the maximum repeatability error was 3.8 cm. We believe that nonlinearity errors were mostly due to strong harmonic distortion in the illumination system.

While the SPSD prototype has exhibited similar error performance achieved by other state-of-the-art 3D imager approaches, the latter have benefited from several years of optimizations [1]–[6]. Continued engineering practice in technology, device, and circuits is expected to highly enhance SPSD over the years following this paper. In particular, significant improvements in distance resolution are expected by improving light detection in pixels. For example, light detection efficiency may be improved by means of microlenses or by enhancing photon-detection probability. While microlenses are readily available, the improvement of SPAD detection efficiency at 850 nm is more challenging. SPAD structures that utilize deeper layers in CMOS could also improve overall performance in SPAD sensors operated in red and near infrared spectral regions.

APPENDIX

In the general case of N_C samples values and any periodic illumination waveform, since the SPSD demodulation may be seen as a synchronous sampling of the incident optical signal, one may utilize the theory of discrete Fourier transform (DFT)

to relate the quantities of interest to the sampled values. In particular, it is assumed for the moment that the number of samples N_C is high enough to satisfy the Nyquist-Shannon sampling theorem for a given illumination waveform. The sampled sequence F_n is

$$F_n = \frac{1}{N_C} \sum_{k=0}^{N_C-1} C_k e^{-i2\pi \frac{n}{N_C} k}. \tag{A.1}$$

Since we want to determine the phase of the first harmonic only, we can determine A', B', and φ in the case of $n = 1$, i.e.,

$$A' = \frac{2}{N_c}\sqrt{\left(\sum_{k=0}^{N_C-1} C_k \cos\left(2\pi\frac{k}{N_C}\right)\right)^2 + \left(\sum_{k=0}^{N_C-1} C_k \sin\left(2\pi\frac{k}{N_C}\right)\right)^2} \tag{A.2}$$

$$B' = \frac{1}{N_C} \sum_{k=0}^{N_C-1} C_k \tag{A.3}$$

$$\varphi = -\arctan\left\{\frac{\Sigma_{k=0}^{N_C-1} C_k \sin\left(2\pi\frac{k}{N_C}\right)}{\Sigma_{k=0}^{N_C-1} C_k \cos\left(2\pi\frac{k}{N_C}\right)}\right\} \tag{A.4}$$

where A' and B' are respectively the amplitude and offset of the sampled waveform, shown on the right-hand side of Fig. 3. Since the SPSD sampling intervals ΔT_i are not infinitesimally small, the amplitude to offset ratio between the incident optical signal and the sampled waveform is not constant. Assuming that the sampling intervals ΔT_i are of constant duration ΔT, then the coefficients $\{C_k\}$ are expressed by a convolution of the incident optical power P_S with a sampling window (*rect* function) over a high number of illumination periods, i.e.,

$$C_k = \frac{\eta_{\mathrm{SPAD}}\lambda_{\mathrm{SG}}T}{hc}\left\{P_S(t) * \mathrm{rect}\left(\frac{t - k\frac{T_0}{N_C}}{\Delta t}\right)\right\} \tag{A.5}$$

where T is the integration time, λ_{SG} is the illumination signal wavelength, and η_{SPAD} is the PDP at λ_{SG}. In (A.5), h and c are respectively Plank's constant and the speed of light. Similarly to photogate lock-in pixels, the SPSD demodulation process is characterized by amplitude demodulation efficiency lower than unity, due to the limited bandwidth involved (i.e., finite ΔT). This demodulation efficiency, known as demodulation contrast, is given by

$$C_D = \mathrm{sinc}\left(\pi\frac{\Delta T}{T_0}\right) \tag{A.6}$$

due to the convolution of a *rect* function with the input signal. Note that, unlike conventional photogate lock-in pixels, the theoretical demodulation contrast C_D is not limited in SPSD by pixel non-idealities. The reason for this is that SPADs have a timing resolution of a few tens of picoseconds, thus the theoretical (sharp) definition of sampling windows applies in practice. In other words, the sampling operation is virtually ideal.

Based on these equations, it is possible to relate the incident optical amplitude and offset, for a sinusoidal illumination, as

$$A = \frac{hc}{\eta_{\mathrm{SPAD}}\lambda_{\mathrm{SG}}T}\frac{A'}{\mathrm{sinc}\left(\pi\frac{\Delta T}{T_0}\right)} \tag{A.7}$$

$$B = \frac{hc}{\eta_{\mathrm{SPAD}}\lambda_{\mathrm{SG}}T}\mathrm{sinc}\left(\pi\frac{\Delta T}{T_0}\right)B'. \tag{A.8}$$

REFERENCES

[1] T. Spirig, P. Seitz, O. Vietze, and F. Heitger, "The lock-in CCD-two-dimensional synchronous detection of light," *IEEE J. Quantum Electron.*, vol. 31, no. 9, pp. 1705–1708, Sep. 1995.

[2] R. Miyagawa and T. Kanade, "CCD-based range-finding sensor," *IEEE Trans. Electron Devices*, vol. 41, no. 10, pp. 1648–1652, Oct. 1997.

[3] R. Lange and P. Seitz, "Solid-state time-of-flight range camera," *IEEE J. Quantum Electron.*, vol. 37, no. 3, pp. 390–397, Mar. 2001.

[4] R. Schwarte, Z. Xu, H. Heinol, J. Olk, and B. Buxbaum, "New optical four-quadrant phase detector integrated into a photogate array for small and precise 3D cameras," *Proc. SPIE—Three-Dimensional Image Capture*, vol. 3023, pp. 119–128, 1997.

[5] C. Bamji and E. Charbon, "Systems for CMOS-compatible three-dimensional image sensing using quantum efficiency modulation," US Patent 6,580,496, Jun. 17, 2003.

[6] S. Kawahito, I. A. Halin, T. Ushinaga, T. Sawada, M. Homma, and Y. Maeda, "A CMOS time-of-flight range image sensor with gates-on-field-oxide structure," *IEEE Sensors J.*, vol. 7, no. 12, pp. 1578–1586, Dec. 2007.

[7] B. Büttgen and P. Seitz, "Robust optical time-of-flight range imaging based on smart pixel structures," *IEEE Trans. Circuits Syst., Reg. Papers*, vol. 55, no. 6, pp. 1512–1525, Jun. 2008.

[8] C. Niclass, A. Rochas, P.-A. Besse, and E. Charbon, "Design and characterization of a CMOS 3-D image sensor based on single photon avalanche diodes," *IEEE J. Solid-State Circuits*, vol. 40, no. 9, pp. 1847–1854, Sep. 2005.

[9] C. Niclass, "Method and arrangement for measuring the distance to an object," US Patent Application 2007/0182949 A1, Aug. 9, 2007.

[10] C. Niclass, C. Favi, T. Kluter, M. Gersbach, and E. Charbon, "A 128 × 128 single-photon imager with on-chip column-level 10b time-to-digital converter array capable of 97 ps resolution," in *IEEE Int. Solid-State Circuits Conf. Dig.*, 2008, pp. 44–45.

[11] C. Niclass, C. Favi, T. Kluter, M. Gersbach, and E. Charbon, "A 128 × 128 single-photon imager with column-level 10-bit time-to-digital converter array," *IEEE J. Solid-State Circuits*, vol. 43, no. 12, pp. 2977–2989, Dec. 2008.

[12] D. V. O'Connor and D. Phillips, *Time-Correlated Single-Photon Counting*. London, U.K.: Academic Press, 1984.

[13] C. Niclass, C. Favi, T. Kluter, F. Monnier, and E. Charbon, "Single-photon synchronous detection," in *Proc. 34th European Solid-State Circuits Conf. (ESSCIRC)*, 2008, pp. 114–117.

[14] R. Lange, "3D time-of-flight distance measurement with custom solid-state image sensors in CMOS/CCD-technology," Ph.D. dissertation, Univ. of Siegen, Siegen, Germany, 2000.

[15] C. Niclass, "Single-photon image sensors in CMOS: picosecond resolution for three-dimensional imaging," Ph.D. dissertation no. 4161, Ecole Polytechnique Fédérale de Lausanne, Lausanne, Switzerland, 2008, Reprint: Hartung-Gorre Verlag, ISBN-10: 3-86628-220-6, ISBN-13: 978-3-86628-220-9, p. 251.

[16] B. Büttgen, "Extending time-of-flight optical 3D-imaging to extreme operating conditions," Ph.D. dissertation, Univ. of Neuchâtel, Neuchâtel, Switzerland, 2006.

Cristiano Niclass (S'05–M'08) received the M.S. degree in microelectronics in 2003 and the Ph.D. degree in electrical engineering and computer science in 2008, both from the Swiss Federal Institute of Technology Lausanne (EPFL).

From 2003 to 2006, he worked as a part-time R&D Engineer for Ingenico (Suisse) SA in the design of electronic payment devices. In May 2003, he joined the Processor Architecture Laboratory of EPFL and subsequently the Quantum Architecture Group, where he worked toward the Ph.D. degree. At EPFL, he has investigated the design, implementation, and characterization of fully integrated image sensors in CMOS using single-photon detectors.

He has also been involved in the design of high-speed and high-resolution data converters implemented in conventional technologies. In 2005, he spent two months with the Information System Laboratory of Stanford University, where he studied conventional image sensors in CMOS. Since March 2009, Dr. Niclass has been with Toyota Central R&D Labs Inc., in Japan, where he holds a Researcher position in the Optical Device and System Laboratory. He has authored or coauthored over 30 peer-reviewed journal and conference publications, and is the inventor or coinventor on seven patent applications. His interests include many aspects of high-speed and low-noise mixed-signal ICs, with emphasis on high-performance imaging.

Claudio Favi received the B.S. and M.S. degrees in electrical engineering from EPFL Lausanne in 2004. Since 2005, he has been pursuing the Ph.D. degree in the AQUA group led by Prof. Charbon. His research interests are optical communications, electronic design automation, and embedded systems.

Theo Kluter received the Master degree in electrical engineering from the Technische Universiteit Twente, Enschede, The Netherlands, in 1996. He worked as an R&D assistant in the Faculty of Computer Controlled Systems and Computer Techniques until 1997. From 1997 to 2002, he was a Design Engineer in the Design Center of Dedris Embedded Systems/Frontier Design/Adelante Technologies, Tiel, The Netherlands. In 2002, he joined Agere Systems as acting interim product development team leader for the Infotainment Group, Nieuwegein, The Netherlands. In June 2003, he joined EPFL, where he currently is pursuing the Ph.D. degree in the Processor Architecture Laboratory (LAP). His research interests include various aspects of embedded computer and processor architecture, embedded multiprocessor system-on-chip, design automation, and application-specific embedded system design.

Frédéric Monnier was born in Lausanne, Switzerland, in 1982. He received the HES Diploma in microtechnology from EIG (Engineering School of Geneva), Switzerland, in 2007. From December 2007 to August 2008, he was a research assistant in the Processor Architecture Laboratory of EPFL. Since August 2008, he has been with the technical staff of the Microsystems Design Group of EPFL. His interests include the design and programming of electronic circuits and microsystems.

Edoardo Charbon (M'92) received the Diploma from ETH Zurich in 1988, the M.S. degree from the University of California at San Diego in 1991, and the Ph.D. degree from the University of California at Berkeley in 1995, all in electrical engineering and computer science.

From 1995 to 2000, he was with Cadence Design Systems, where he was responsible for analog and mixed-signal design automation tools and the architect of the company's initiative for intellectual property protection. In 2000, he joined Canesta Inc. as its Chief Architect, leading the development of wireless 3-D CMOS image sensors. In November 2002, he joined the Faculty of EPFL in Lausanne, Switzerland, working in the field of CMOS sensors, biophotonics, and ultra low-power wireless embedded systems. In Fall 2008, he joined the Faculty of TU Delft, as a full Professor in VLSI design. He has consulted for numerous organizations, including Texas Instruments, Hewlett-Packard, and the Carlyle Group. He has published over 100 articles in technical journals and conference proceedings and two books, and he holds nine patents. His research interests include high-performance imaging, quantum integrated circuits, and design automation algorithms.

Dr. Charbon has served as a Guest Editor of the IEEE TRANSACTIONS ON COMPUTER-AIDED DESIGN OF INTEGRATED CIRCUITS AND SYSTEMS and the IEEE JOURNAL OF SOLID-STATE CIRCUITS, and as Chair of technical committees in ESSCIRC, ICECS, ISLPED, and VLSI-SOC.